Solid State Phenomena
ISSN: 1662-9779, Vol. 389, pp 115-123
doi:10.4028/p-0SlKmg

Submitted: 2025-12-26
Revised: 2026-02-20
Accepted: 2026-02-24
Online: 2026-04-16

Numerical Modeling of Controlled Multi-Step Expansion in Plasma Arc Welded AISI 316 Stainless-Steel Tubes

BORDA Francesco[1,a], CARUSO Serafino[1,b*] and FILICE Luigino[1,c]

[1]Department of Mechanical, Energy and Management Engineering, University of Calabria, 87036 Rende, CS, Italy

[a]francesco.borda@unical.it, [b]serafino.caruso@unical.it, [c]luigino.filice@unical.it
(*corresponding author)

Keywords: Plasma arc welding; controlled tube expansion; AISI 316 stainless steel; multi-step expansion; finite element modeling.

Abstract. The increasing demand for reliable and high-performance heat-transfer components has stimulated the development of robust joining and forming strategies for thin-walled stainless-steel tubes. In this work, the Controlled Tube Expansion of Plasma Arc Welded AISI 316 stainless-steel tubes was investigated through a combined experimental and numerical approach. Welded tubes with an initial diameter of 130 mm were expanded to 180 mm using a three-step mechanical expansion process, and six different expansion sequences were experimentally evaluated. Finite element simulations were performed using a coupled thermo-mechanical model incorporating a damage-based fracture criterion to predict material failure during expansion. Numerical predictions were in good agreement with experimental observations and allowed the identification of a critical cumulative damage threshold governing tube failure. Based on these results, a processability domain was defined, clearly distinguishing safe and unsafe expansion paths. The study demonstrates that tube expandability is strongly dependent on the deformation path and highlights the importance of progressive expansion strategies for maximizing material ductility while preventing fracture.

Introduction

The growth in demand for high-performance heat-transfer systems has intensified the demand for reliable and efficient joining techniques for stainless-steel tubes, especially those produced from AISI 316 [1-3]. Among the existing welding technologies, Plasma Arc Welding (PAW) has emerged as a key enabling process due to its superior stability, high energy density, and ability to produce narrow and deeply penetrating welds [4-6]. These characteristics are of paramount importance for applications involving Controlled Tube Expansion (CTE), where weld integrity plays a decisive role in ensuring both the quality of the expanded joint and the overall structural reliability of the system [7-9]. Minor imperfections in the PAW weld, such as lack of fusion, overheating, or microstructural inhomogeneities, can significantly reduce the ductility of the tube and compromise its response during mechanical expansion. Despite the broad industrial relevance of CTE processes, predicting the risk of tube failure during expansion remains of considerable challenge. The material is subjected to complex deformation paths and the failure process is dominated by interactions between weld geometry, thermally affected microstructures, and multiaxial stress states. To address these difficulties, numerical simulations based on the Finite Element Method (FEM) have become indispensable tools. FEM allows for detailed reproduction of the expansion mechanics and provides access to stress and strain fields that are difficult or impossible to measure experimentally [10-12]. A central aspect of such simulations involves an accurate fracture criterion capable of predicting the onset of damage and rupture under the specific loading path imposed by the expansion process [13-15]. The proper prediction of this criterion is essential not only to determine optimal process steps for obtaining defect-free expanded tubes but also to define a robust processability domain. This domain delineates safe expansion conditions, where tube integrity is preserved, from unsafe regimes leading to failure. Ultimately, the integration of PAW process characterization with advanced FEM modeling provides a powerful framework for enhancing process reliability, reducing trial-and-error experimentation, and improving the design of next-generation mechanically expanded tube–sheet joints.

Experimental Procedure

PAW experiments were carried out on AISI 316 stainless steel (Table 1) using an automated torch system (SITEC BSL 1000 LTC) equipped with a THERMAL ARC 4A DUAL FLOW TORCH. The welding was performed on 0.5 mm thick sheets, subsequently folded and joined to produce tubes with an initial diameter of 130 mm and a length of 200 mm, as shown in Fig. 1a.

Table 1. Nominal chemical composition of AISI 316 stainless steel (wt.%)

Elements	Cr	C	Mn	Si	Ni	P	S	Mo	Cu	Fe
Weight %	16.8	0.016	1.44	0.218	10.1	0.031	0.023	2.01	0.418	Balance

Welding parameters included a current of 115 A, a welding speed of 69.33 mm/s, and a plasma gas flow rate of 15 L/min, while Argon was supplied as shielding gas at 4 L/min.

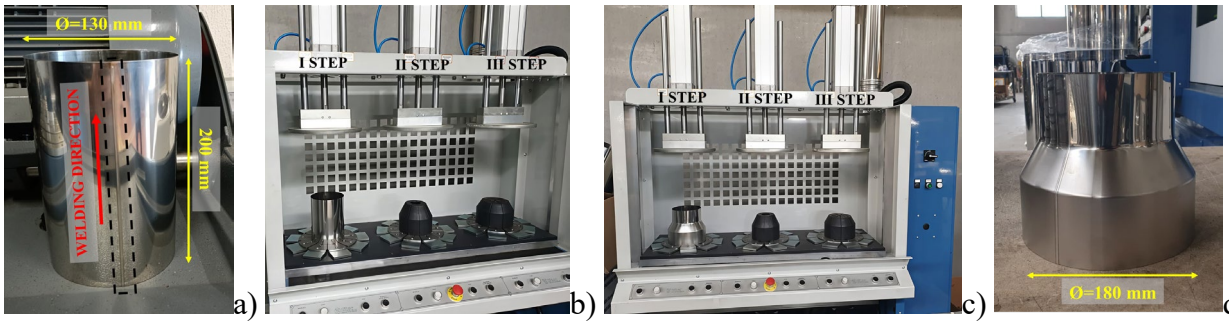

a) b) c) d)

Fig. 1. Experimental procedure for tube expansion: a) initial welded tube; b) positioning of the tube on the first expansion station; c) tube at the end of the first expansion step; d) fully expanded tube after the third expansion step.

After fabrication, the tubes were expanded from 130 mm to 180 mm using a SITEC expansion machine (Figs. 1b - 1c) to manufacture components intended for aeration systems (Fig. 1d). The expansion system consists of three sequential stations specifically designed to perform the diameter increase in three controlled steps, thereby reducing the risk of excessive deformation that would likely occur if the entire expansion were executed in a single pass. Each station includes eight identical Teflon dies (black elements in Figs. 1b-1c), which move at an expansion speed of 0.74 mm/s. Although identical in number, the die geometries vary from station to station to achieve a progressive deformation of the tube. Additionally, each station is equipped with an upper flat punch that prevents upward displacement of the tube during expansion, a phenomenon that may occur due to the process kinematics. To determine the optimal sequence of diameter increments for obtaining defect-free expanded tubes while defining a robust processability domain, six experimental cases with different expansion sequences were investigated, as summarized in Table 2.

Table 2. Experimental plan for the multi-step tube expansion process

Process procedure	Diameter expansion [mm]		
	I Step	II Step	III Step
1	10	10	30
2	10	20	20
3	10	30	10
4	20	10	20
5	20	20	10
6	30	10	10

For statistical robustness and to ensure the reliability of the results, three replications were performed for each test condition, yielding a total of eighteen experiments conducted in randomized order. This approach also strengthens the subsequent numerical analysis of the fracture criterion and supports the definition of a reliable processability window.

Analysis of the six proposed procedures for expanding the tubes from 130 mm to 180 mm clearly indicates that only procedure 2 successfully achieves the target diameter in a technologically sound manner, Figure 2. Although all procedures reach the required 50 mm total expansion, several of them exhibit poorly balanced deformation increments, with excessively large initial or final steps that may induce material instability, ovalization, or surpass the operational limits of the equipment. Certain sequences focus the deformation at one step of 30 mm, while others introduce too large an increment during the initial stage, which hampers the smooth progression required for deformation. In contrast, procedure 2, which involves equal increments of 10, 20, and then 20 mm deformation, provides an equal and measured share of deformation at the three stations. Thus, this pattern avoids mechanical instabilities and promotes better control during the processes, as it is the only procedure that can successfully deform the sample from 130 mm to 180 mm. These experimental outcomes are particularly valuable for analyzing the fracture criterion employed in the numerical modelling. They provide reliable data on the material's deformation limits and on the conditions beyond which the tube can no longer withstand the imposed diameter increase. The subsequent FE simulations will enable detailed investigation of the material damage evolution at each expansion step, offering a scientific explanation for the observed failure modes and allowing for a more accurate definition of the feasible processing domain for the expansion operation.

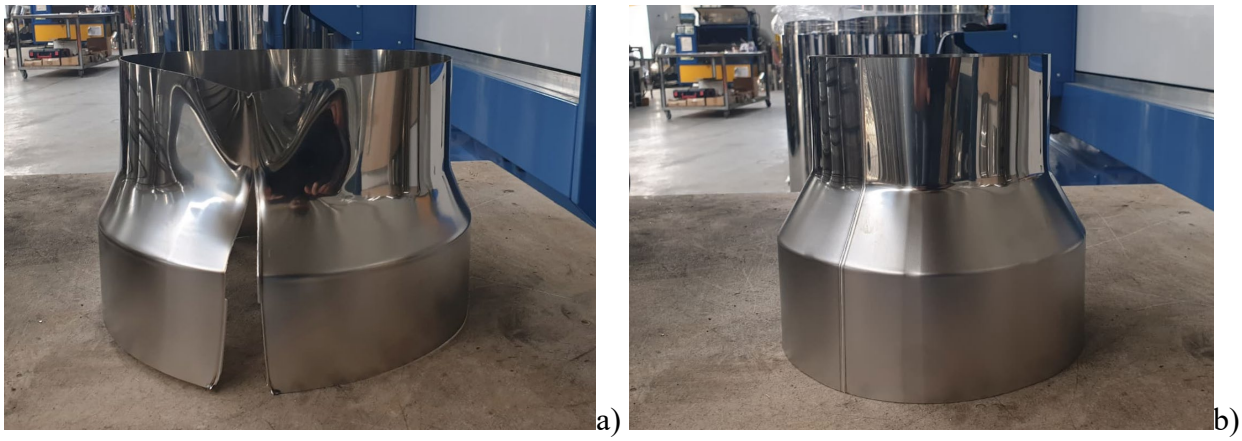
a) b)

Fig. 2. Comparison of tube expansion outcomes for two experimental procedures: a) failure observed for the 10–10–30 mm sequence; b) successful expansion for the 10–20–20 mm sequence.

Finite Element Modeling of Tube Expansion

The commercial FE software DEFORM-2D™ SFTC was employed to simulate the CTE process through a coupled thermo-mechanical analysis performed in a two-dimensional axisymmetric framework reproducing the experimental expansion configuration. The workpiece was discretized into 12,000 elements and modeled as a plastic material with isotropic hardening. Each station's die was modeled as a rigid body consisting of 1,200 elements, as illustrated in Fig. 3. Regarding the kinematic boundary conditions, an expansion speed of 0.74 mm/s, consistent with the experimental procedure, was imposed on the die, allowing translation along the X direction while constraining motion in the Y direction.

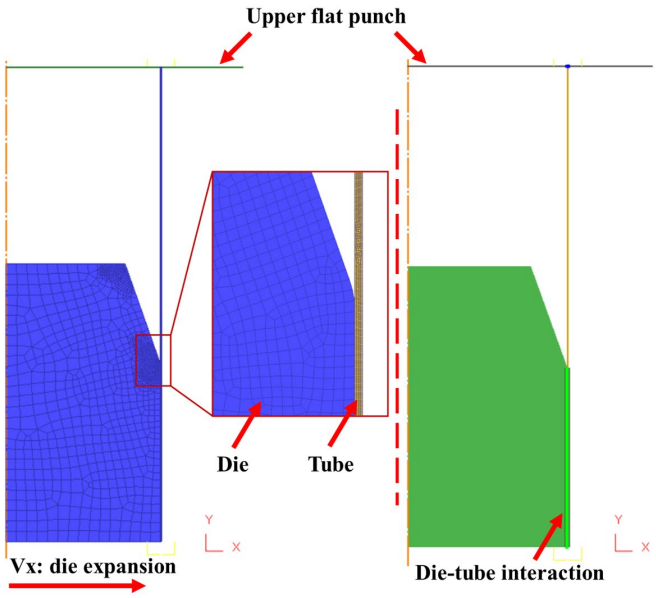

Fig. 3. Finite element model of the tube expansion process: axisymmetric mesh of the tube and dies and die–tube interaction setup.

The tube was also constrained in the +Y direction movement, reflecting the experimental use of an upper flat punch that prevents upward displacement during the expansion process. The die–tube interaction was described using a sliding friction formulation based on the Coulomb law, $\tau=\mu\sigma_n$, where σ_n is the normal stress at the die-tube interface, and $\mu=0.05$ is the local friction coefficient, determined from available data between Teflon (die) and AISI 316 stainless steel (tube) and calibrated through consistency between numerical results and experiments. Tube failure during expansion was modeled using the Brozzo et al. [16] fracture criterion, which accounts for the influence of hydrostatic stress, as expressed in Eq. (1):

$$\int_0^{\bar{\varepsilon}_f} \frac{2\sigma_1}{3(\sigma_1-\sigma_m)}\, d\bar{\varepsilon} = D \tag{1}$$

where ε_f is the effective strain at failure, σ_1 the principal stress, σ_m the hydrostatic stress and D the material damage constant. The material flow stress was described using the tabular data format $\sigma(\varepsilon, \dot{\varepsilon}, T)$ available in DEFORM-2D™ SFTC, which expresses flow stress as a function of effective strain, strain rate and temperature.

Results and Discussion

By means of the FEM, it was possible to accurately reproduce the tube expansion process, predicting the evolution of the mechanical behavior of the workpiece and providing a sound mechanical interpretation of the corresponding experimental results. Figure 4 shows the good agreement between numerical predictions and experimental results for Procedure 1 (10–10–30). In particular, the model accurately identifies the critical zone, which coincides with the fracture location observed experimentally.

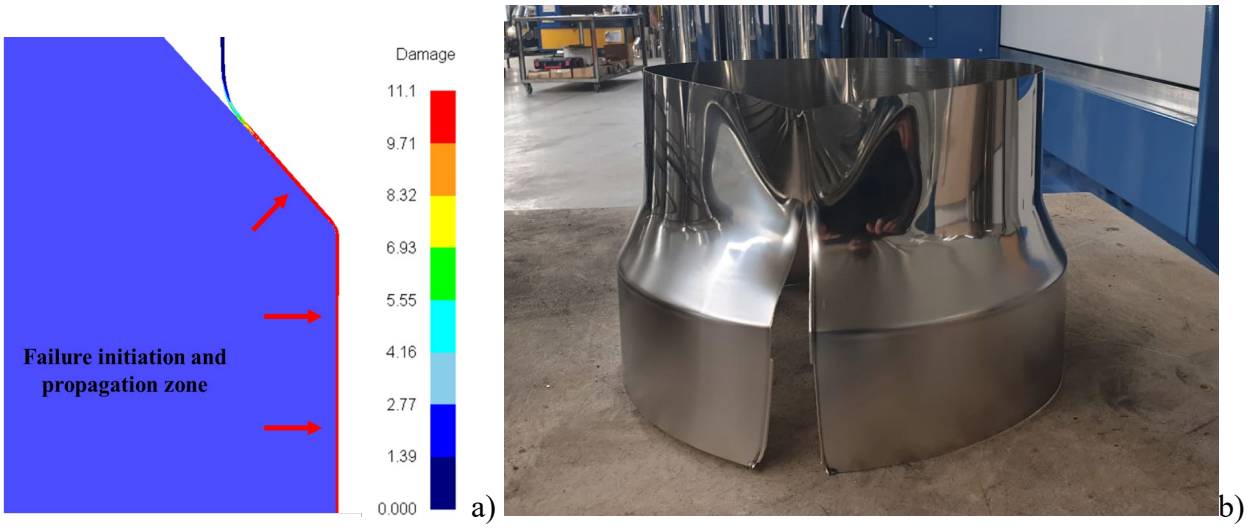

Fig. 4. Numerical–experimental comparison of tube expansion results for the 10–10–30 mm loading sequence: a) predicted damage distribution and b) experimentally observed fracture location.

Thanks to the numerical framework and to the implementation of the fracture criterion, the underlying mechanical mechanisms governing the success or failure of the expansion process could be investigated in greater depth. This approach enabled the identification of the fundamental factors controlling damage accumulation and, consequently, the definition of the optimal expansion steps required to obtain defect-free expanded tubes. In particular, the numerical analysis made it possible to start from the only experimentally identified safe process procedure (the No. 2 in Table 2) with diameter increments of 10–20–20 mm, which is the sole sequence capable of achieving complete tube expansion without fracture, and to systematically analyze all alternative procedures, providing a clear mechanical explanation for why they inevitably lead to failure.

Table 3 reports the evolution of cumulative damage predicted during the three-step tube expansion process, clearly demonstrating that the sequence of diameter increments plays a decisive role in determining the structural integrity of the tube.

Table 3. Numerical prediction of cumulative damage during the multi-step tube expansion process

Process procedure	Damage value		
	I Step	II Step	III Step
1 (10-10-30)	0.11	0.15	11.10
2 (10-20-20)	0.11	1.98	2.75
3 (10-30-10)	0.11	7.32	7.83
4 (20-10-20)	1.10	1.92	4.91
5 (20-20-10)	1.10	3.89	3.95
6 (30-10-10)	1.80	2.85	2.89

Considering the experimental results, the finite element analysis indicates that only the 10–20–20 mm expansion procedure successfully completes the tube expansion without inducing material damage, whereas all other sequences lead to cumulative damage levels exceeding the material's integrity threshold. Notably, all failed procedures reach cumulative damage values above 2.75, which defines the critical threshold for fracture. In contrast, the 10–20–20 mm sequence reaches a maximum cumulative damage of 2.75 at the end of the third step, indicating that the material is fully utilized without approaching its ductility limit. These findings confirm that failure is directly associated with exceeding a critical damage threshold rather than occurring randomly.

Mechanically, the first expansion step is crucial in defining the residual deformability of the tube. An initial diameter increase of 10 mm produces minimal damage, allowing for progressive and homogeneous plastic deformation in subsequent steps. In procedures with larger initial expansions of 20 or 30 mm, significant early-stage damage substantially reduces residual ductility, predisposing the tube to premature failure. In the 10–20–20 mm sequence, damage accumulates gradually and evenly

throughout the process, preventing excessive strain localization and enabling stable strain hardening. This controlled deformation delays the nucleation and coalescence of microvoids responsible for ductile fracture. Conversely, in alternative sequences, damage is highly concentrated in a single expansion step, rapidly exceeding the critical threshold. Excessive increments applied at intermediate or final stages impose deformation levels that the material cannot accommodate, even if earlier steps are mild.

Overall, the results demonstrate strong internal consistency and physical significance. All expansion strategies exceeding the critical damage value of 2.75 lead to tube failure, whereas the 10–20–20 mm sequence fully exploits the material's ductility without surpassing the fracture limit. Based on these findings, a robust processability domain was defined (Figure 4), clearly delineating safe expansion conditions, where tube integrity is preserved, from unsafe regimes leading to inevitable material failure.

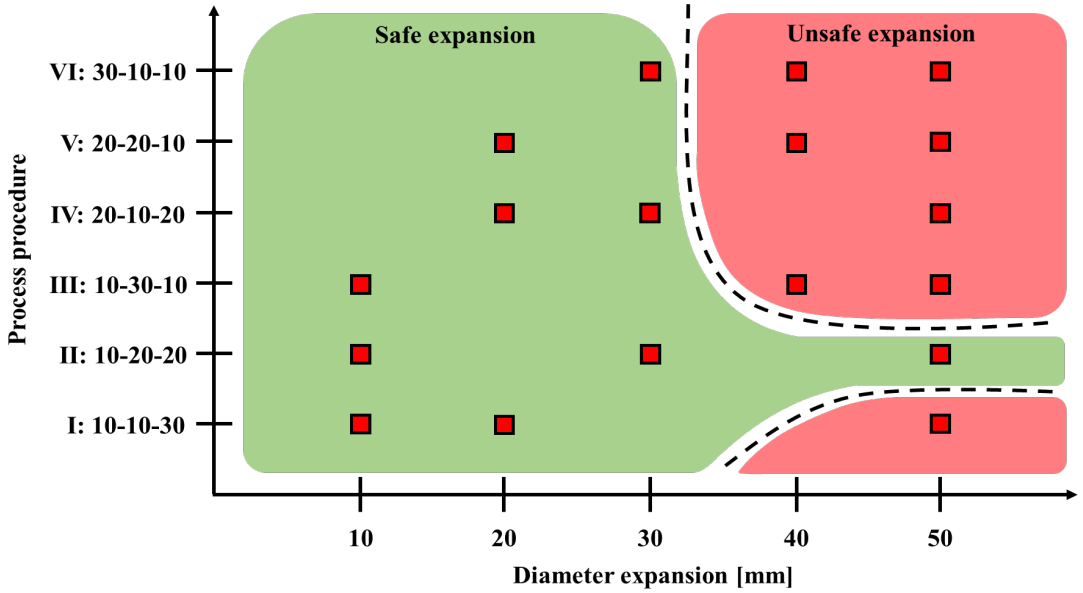

Fig. 4. Processability domain for multi-step tube expansion, showing safe (green) and unsafe (red) deformation regimes. The 10–20–20 mm expansion path lies entirely within the safe region, illustrating a progressive and damage-controlled deformation strategy.

Figure 4 provides a concise representation of the processability domain obtained from the combined experimental and numerical investigation. The region of safe and unsafe expansion strategies has been pointed out in this diagram, showing not only the dependence of tube expandability on the total extent of expansion but also the pathway of deformation used. The region has been coloured differently to make it distinct, and this includes the region of safe expansion, which has been coloured green, while the other has been coloured light red. Inside the green safe region, deformation is increasingly and controlled, and this provides the material the opportunity to resist high plastic strain without embarking on unstable processes of failure. The 10–20–20 mm expansion path lies entirely within this region, confirming that an initially mild deformation step is critical to preserve sufficient residual ductility for subsequent expansions. From a micromechanical perspective, this behavior reflects the gradual evolution of void nucleation and growth, which remains stable as long as strain localization is avoided and the material's hardening capacity is not prematurely exhausted. In contrast, all other investigated procedures intersect the light red unsafe region, as they involve diameter increments that induce excessive damage at one or more stages. In these cases, localized plastic flow dominates the material response, accelerating void coalescence and resulting in ductile fracture. The processability domain also provides predictive capability. Instead of relying on trial-and-error experimentation, it offers a rational framework for designing expansion schedules that maximize formability while minimizing the risk of fracture. By constraining each expansion step within the green safe region, the material's ductility can be fully exploited in a repeatable and reliable

manner, which is particularly relevant for industrial applications requiring robust and defect-free processes. Finally, the fact that the safe and unsafe regions are clearly demarcated confirms the preeminent importance of damage-controlled fracture in the process. This confirms the appropriateness of the fracture criterion chosen, the importance of the finite element simulations, as well as the accuracy of the proposed methodological approach for modeling the process of tube expansion. Figure 4 thus summarizes the key findings of this work, presenting an intuitive processability map that identifies a unique safe expansion path and a well-defined damage threshold, offering both scientific insight and practical guidance for the design of multi-step tube expansion processes.

Conclusions

This work presents a comprehensive experimental–numerical investigation of the Controlled Tube Expansion of PAW-welded AISI 316 stainless-steel tubes, with the aim of identifying reliable expansion strategies and defining a robust processability domain. The main conclusions can be summarized as follows:

- the results indicate that, in PAW-welded AISI 316 material tubes, the effect of the sequence of diametric expansion increments is significantly greater than that of total expansion. The weld path can appreciably influence damage and subsequent failure modes when different deformation processes, leading to identical final diameters, are considered;
- among the analyzed procedures, only the 10–20–20 mm size increment pattern was successful in reaching the desired size without breakage. Such a method helps increase plastic deformation evenly;
- finite element simulations incorporating a damage-based fracture criterion revealed the presence of a critical cumulative damage value of approximately 2.75. All expansion routes exceeding this critical damage resulted in material failures that confirmed that material fracture is a function of damage rather than instability;
- with the combined experimental-numerical approach, it has become possible to define the domain of processability, which distinguishes without ambiguity the areas of expansion conditions as being either safe or unsafe. This domain can be efficiently used in the design of processes involving multiple steps in tube expansion.

Acknowledgments

The authors gratefully thank Dott. G. Mezzatesta of Profiltek s.r.l. (Italy) for its valuable contribution to the research.

References

[1] M. Radha Raman, T. Visnu, S. Rajesha, A Study of Tensile Strength of MIG and TIG Welded Dissimilar Joints of Mild Steel and Stainless Steel, IJASME. 3 (2014) 23-32. https://doi.org/10.14810/ijamse.2014.3203.

[2] S. Manabendra, S. Dhami, Effect of TIG Welding Parameter of Welded Joint of Stainless Steel SS304 by TIG Welding, SSRN. (2020). http://dx.doi.org/10.2139/ssrn.3643709.

[3] H. Vinoth Kumar, M. Balakrishnan, K. Gulanthaivel, R. Logeshwaran, R. Mohanraj, Investigation on effects of flux assisted GTAW welding process on mechanical, metallurgical characteristics of dissimilar metals SS 304 and SS 316 L, Mater. Today Proc. 33 (2020) 3191-3196. https://doi.org/10.1016/j.matpr.2020.04.143.

[4] M. Samiuddin, J. Li, M. Taimoor, M.N. Siddiqui, S.U. Siddiqui, J. Xiong, Investigation on the process parameters of TIG-welded aluminum alloy through mechanical and microstructural characterization, Def. Technol. 17 (2021) 1234-1248. https://doi.org/10.1016/j.dt.2020.06.012.

[5] G. Rotella, M.Sanguedolce, M.R. Saffioti, L. Filice, F. Testa, Strategies for Shaping of Different Ceramic Foams, Proc. Manuf. 47 (2020) 493-497. https://doi.org/10.1016/j.promfg.2020.04.345.

[6] A. Del Prete, L. Filice, D. Umbrello, Numerical Simulation of Machining Nickel-Based Alloys. Proc. CIRP. 8 (2013) 540-545, https://doi:10.1016/j.procir.2013.06.147.

[7] F. Borda, A.M.I. Cosma, L. Filice, Enabling Industry 4.0 Transformation in Calabria region: Framework, Machine Interconnection and ERP Synergy, Procedia Comput. Sci. 232 (2024) 1151-1163. https://doi.org/10.1016/j.procs.2024.01.113.

[8] F. Borda, A.D. La Rosa, L. Filice, F. Gagliardi, Environmental comparison of opposing manufacturing strategies at changing of energy sources, EoL approaches and shape peculiarity for an automotive component, Adv. Mater. Process. Technol. (2024) 1-21. https://doi.org/10.1080/2374068X.2024.2432724.

[9] M. Sanguedolce, G. Rotella, M.R. Saffioti, L. Filice, Burnishing of AM materials to obtain high performance part surfaces, JIEM. 15 (2022) 73-89. https://doi.org/10.3926/jiem.3608.

[10] A.A. Deshpande, L. Xu, W. Sun, D.G. McCartney, T.H. Hyde, Finite-element-based parametric study on welding-induced distortion of TIG-welded stainless steel 304 sheets. J. Strain Anal. Eng. Des. 46 (2011) 267-279. doi:10.1177/0309324711398763.

[11] S. Caruso, E. Sgambitterra, S. Rinaldi, A. Gallone, L. Viscido, L. Filice, D. Umbrello, Experimental comparison of the MIG, friction stir welding, cold metal transfer and hybrid laser-MIG processes for AA 6005-T6 aluminium alloy, AIP Conf. Proc. 1769 (2016) 100004. https://doi.org/10.1063/1.4963498.

[12] M. Seyyedian, M. Haghpanah, M. Sedighi, Investigation of the effect of clamping on residual stresses and distortions in butt welded plates, Sci. Iranica Trans. B. Mech. Eng. 17 (2010) 387-394.

[13] D.R. Behera, P.S. Lin Prakash, P. Kundu, R.R. Kumar, S.V.S.N. Murty, S.K. Kar, S.K. Panda, Microstructure Characterization and Formability Assessment of Electron Beam Welded Nb-10Hf-1Ti (Wt.%) Refractory Alloy Sheets. Int. J. Refract. Met. Hard Mater. 125 (2024) 106912. https://doi.org/10.1016/j.ijrmhm.2024.106912.

[14] J. Xie, A. Kar, Laser welding of thin sheet steel with surface oxidation, Weld J. 78 (1999).

[15] K.H. tseng, Y.C. Chen, Micro Plasma Arc Welding of AM 350 Precipitation Hardening Alloys, Appl. Mech. Mater. (2011) 121-126. https://doi.org/10.4028/www.scientific.net/AMM.121-126.2681.

[16] X. Li, J. Liang, T. Shi, D. Yang, X. Chen, C. Zhang, Z. Liu, D. Liu, Q. Zhang, Tribological Behaviors of Vacuum Hot-Pressed Ceramic Composites with Enhanced Cyclic Oxidation and Corrosion Resistance. Ceram. Int. 46 (2020) 12911–12920. https://doi.org/10.1016/j.ceramint.2020.02.057.

[17] S. Caruso, D. Umbrello, Numerical and experimental validation of gas metal arc welding on AISI 441 ferritic stainless steel through mechanical and microstructural analysis. Int. J. Adv. Manuf. Technol. 120 (2022) 7433–7444. https://doi.org/10.1007/s00170-022-09208-x.

[18] F. Rubino, F. Tucci, S. Caruso, D. Umbrello, P. Carlone, An integrated numerical approach to simulate the filler deposition and the shape distortions in gas metal arc welding, CIRP J. Manuf. Sci.Technol. 45 (2023) 26-34, ISSN 1755-5817, https://doi.org/10.1016/j.cirpj.2023.05.010.

[19] Y. Rong, G. Mi, J. Xu, Y. Huang, C. Wang, Laser penetration welding of ship steel EH36: a new heat source and application to predict residual stress considering martensite phase transformation. Mar. Struct. 61 (2018) 256–267. https://doi.org/10.1016/j.marstruc.2018.06.003.

[20] Y.C. Huang, C.H. Su, S.K. Wu, C. Lin, A Study on the Hall–Petch Relationship and Grain Growth Kinetics in FCC-Structured High/Medium Entropy Alloys. Entropy. 21 (2019) 297. https://doi.org/10.3390/e21030297.

[21] J. Moravec, I. Novakova, J. Sobotka, H. Neumann, Determination of Grain Growth Kinetics and Assessment of Welding Effect on Properties of S700MC Steel in the HAZ of Welded Joints. Metals 9 (2019) 707. https://doi.org/10.3390/met9060707.

[22] R.M. German, Grain Growth in Austenitic Stainless Steels. Metallography 11(1978) 235–239, doi:10.1016/0026-0800(78)90043-5.